The end of the isotopic evolution of atmospheric xenon

L. Ardoin, M.W. Broadley, M. Almayrac, G. Avice, D.J. Byrne, A. Tarantola, A. Lepland, T. Saito, T. Komiya, T. Shibuya, B. Marty

Supplementary Information

The Supplementary Information includes:

- ➢ Geological Context
- ➢ Materials and Methods
- ➢ Fluid Inclusions Study
- ➢ Fissiogenic and Mantle Contribution
- ➢ Tables S-1 to S-4
- ➢ Figures S-1 to S-4
- ➢ Supplementary Information References

Geological Context

Hydrothermal quartz samples were selected from two different cratons based on their ages of formation, between 2.3 and 2.5 Ga, encompassing the GOE (Holland, 2006; Lyons *et al.*, 2014; Gumsley *et al.*, 2017). The Ongeluk Formation is a succession of pillowed and sheeted andesitic basalts that has undergone alteration with temperatures not exceeding 200 °C and metamorphism up to prehnite-pumpellyite facies (Cornell *et al.*, 1996; Gutzmer *et al.*, 2001, 2003). This formation is intercalated with the Makganyene glaciation deposits formed during one of the Paleoprotezoic snowball earth events (Evans *et al.*, 1997). Pods of quartz formed within the open spaces of the pillows soon after the eruption as indicated by the lack of deformation in the cavities (Gutzmer *et al.*, 2003; Saito *et al.*, 2016). The pillow-lavas are considered to have formed 2425.6 ± 2.6 Ma (2σ; Gumsley *et al.*, 2017) and give an upper bound to the sample. Saito *et al.*, (2018) performed Ar-Ar dating on three distinct quartz pods to estimate when the quartz crystals precipitated. They

found a maximum age of 2701 ± 43 Ma (1σ) and a minimum age of 2114 ± 312 (1σ) Ma. The difference is likely due to the difficulties in estimating the initial amount of K in the fluid. The age of ≈ 2701 Ma is unlikely given the age of the host rock. The petrographic description of the fluid inclusion indicates a predominantly primary origin (Saito *et al.*, 2018). Thus, the minimum age of the trapped atmospheric noble gases within the inclusions is relative to the quartz pods formed at 2114 ± 312 Ma, consistent with the upper bound of the pillow lava formation.

The Seidorechka (sample FD1A) and Polisarka (sample FD3A) sedimentary formations are part of the Imandra-Varzuga Greenstone Belt. These formations were targeted by the Fennoscandian Artic Russia – Drilling Early Earth Project (FAR-DEEP; Melezhik *et al.*, 2013) of the International Continental Scientific Drilling Program. The Imandra-Varzuga Greenstone Belt consist of several successions of alternating thin sedimentary and thick volcanic formations overlying the Archean basement (Melezhik and Sturt, 1994; Warke *et al.*, 2020). Hydrothermal quartz was collected from veins cross-cutting solely these sedimentary formations, in the shale member for FD1A and in the diamictite-greywacke member for FD3A. Depositional ages of Seidorechka and Polisarka sedimentary formations have been constrained between 2501.5 ± 1.7 Ma and 2441 ± 1.6 Ma (Amelin *et al.*, 1995), and 2441 ± 1.6 Ma and 2434 ± 6.6 Ma (Brasier *et al.*, 2013), respectively. We assumed that minerals contained in quartz veins formed contemporaneously with the overlying volcanic formations that define the minimum age of these sedimentary formations and thus yield ages of 2441 ± 1.6 Ma for the quartz veins crossing Seidorechka Sedimentary Formation (FD1A ; Amelin *et al.*, 1995) and at 2434 ± 6.6 Ma for the quartz veins crossing Polisarka Sedimentary Formation (FD3A ; Brasier *et al.*, 2013).

Materials and Methods

For noble gas analyses, quartz grains of 2 to 4 mm in size were handpicked under a binocular microscope and loaded into hand-activated crushers under vacuum. Gases were extracted using a 3.5 Nm torque wrench to activate each crusher. Purified Ar and Xe gas fractions were measured using a Thermofisher Helix MC Plus© mass spectrometer at CRPG. A total of 9 Ar and Xe analyses were performed on the Ongeluk quartz using the method of Avice *et al.* (2018) that consisted of replicated analyses on distinct crushes of 1 to 3 g of quartz. The Ar isotopic ratios were systematically analysed after each crush to check for the absence of atmospheric contamination. A new technique was used to study samples from the Kola Craton (Péron and Moreira, 2018). It consists of accumulating the extracted gases after crushing steps in an empty and previously evacuated steel bottle immersed in liquid nitrogen (77 K) during 10 minutes before purification and analysis. This method allowed the crushers to be recharged multiple times with fresh quartz grains and therefore enables the Ar and Xe gas fractions to be concentrated within the bottle. By using this method, we prepared 3 bottles for analyses: two bottles by crushing 16.70 g (FD1A-B1) and 10.08 g (FD1A-B2) of sample FD1A in 4 and 3 crusher loads respectively, and one bottle by crushing 18.16 g of sample FD3A in 4 separate crusher loads. The two

different bottles of FD1A extracted gases (FD1A – B1 and FD1A – B2) permitted the analysis of 4 and 5 aliquots of gas, respectively, to ensure reproducibility of the measurements. One bottle of extracted gases from FD3A permitted the analyses of 4 aliquots (Table S-3). The Ar abundance and isotopes were analysed only in the first gas aliquot for each bottle by multicollection. Isotopic ratios of Xe presented in Table 1 are weighted averages of the replicated analyses for each sample. For each sample, we estimated the potential mass-dependent fractionation of Xe (MDF-X, in permille per atomic mass unit ‰.u^{-1}, where a value of 0 indicates no MDF-Xe relative to modern atmospheric Xe) by computing linear regressions on ^{124,126,128}Xe/^{130}Xe isotope ratios using the IsoplotR software (Vermeesch, 2018). Data are given with uncertainties at 2σ.

Fluid inclusions Study

Petrography

Rocks of Seidorechka and Polisarka sedimentary formations are respectively crossed by 3 pluri-centimetric (5 to 10 cm) hydrothermal quartz veins. These veins are restricted to each sedimentary formation and formed after sedimentation. In these volcano-sedimentary deposits (Melezhik *et al.*, 2013), it is likely that the main fluid circulations are linked to the deposit of volcanic units overlying the sedimentary units. Thus, it is assumed that hydrothermal circulations are linked to the accumulation of Seidorechka and Polisarka volcanic formations overlying both sedimentary formations. Fluid inclusions were studied using 200-μm doubly polished thick sections.

Sample FD1A from Seidorechka sedimentary formations does not present obvious quartz recrystallisation but shows a general pattern of parallel trails of fluid inclusions confined within individual grains. At the grain scale, inclusions are either isolated or organised within parallel trails that do not cross grain boundaries (Fig. S-1). The boundaries between grains are decorated by fluid inclusions of less than 5 μm. The interior of the grains contains bigger inclusions, up to 20 μm, that allowed microthermometry and Raman analyses. The inclusions are thus considered primary in origin if they are isolated or pseudo-secondary when organised in trails within the grain structure, in any case trapped during quartz growth (Roedder, 1984). All the inclusions in FD1A are biphasic with the fraction of the bubble in the range 10–20 % of the total volume. Between 5 and 10 % of the inclusions are characterised by the typical CO_2 double bubble feature at room temperature (*e.g.,* Diamond, 2003).

Petrography of fluid inclusions in FD3A from Polisarka sedimentary formation is complex due to quartz deformation and recrystallisation, which resulted in (i) undulose extinction under microscope and (ii) formation of newly recrystallised grains, over ~15 % of the studied thin-section, depleted in fluid inclusions (Fig S-1; Kerrich, 1976). Given the scarcity of 1 to 5 μm fluid inclusions within recrystallised quartz, the recrystallisation has a negligible effect on noble gas analyses compared to non-recrystallised quartz grains where most of fluid inclusions are observed. In the

latter, inclusions can be isolated, organised as trails confined within grains or as decorating quartz sub-grain boundaries. These observations are coherent with a continuous fluid entrapment contemporaneous with formation and deformation of host quartz (Eglinger *et al.*, 2014). No evidence of secondary fluid inclusions was observed. Liquid monophasic and biphasic inclusions about 10 to 20 μm may coexist within the same grain (Fig. S-1). The volume of the vapour bubbles in biphasic inclusions varies from 80 to 20 % of the volume.

Methods

Microthermometry was performed on fluid inclusions from samples FD1A and FD3A using a Linkam MDS600 heating-cooling stage at GeoRessources laboratory (Nancy, France). The following phase transition temperatures were measured when possible: final melting of the carbonic phase (T_m car), apparent first melting of the aqueous phase (T_{fm}), ice melting (T_m ice), clathrate dissociation (T_m cla), partial homogenisation of the carbon-dominated phase (T_h car) and bulk homogenisation of the entire inclusion (T_h). Microthermometry experiments were made between –150 °C and not above 200 °C to avoid decrepitation. The microthermometric stage was calibrated daily using natural pure CO_2 (–56.6 °C) and synthetic pure H_2O fluid inclusions with known transition temperatures. Precisions of the phase transition temperature measurements are about ± 2 °C for T_{fm}, ± 0.1 °C for T_m car, T_m ice, T_{fm}, and T_m cla, and ± 1 °C for T_h.

Raman spectra were acquired at room temperature using a LabRAM HR spectrometer (Horiba Jobin Yvon) equipped with an 1,800 gr.mm^{-1} grating and an edge filter at GeoRessources laboratory (Nancy, France). Excitation was provided by an Ar^+ laser operating at a wavelength of 514.53 nm focussed through a ×50 objective (Olympus). The aperture of the focal hole and the slit were 500 μm and 100 μm respectively. A total of 3 acquisitions were accumulated for each spectrum and acquisition time was variable between 60 and 10 s depending on the quality of the signal and the mobility of the bubble (shorter acquisition time for moving bubble). Spectrum acquisition was systematically performed in the quartz matrix nearby the inclusion of interest at the same depth and same analytical conditions in order to distinguish between N_2 from air and N_2 from the inclusion. Biphasic fluid inclusions often exhibited moving gas bubbles which prevented the acquisition of the Raman spectra. Spectra of CH_4, H_2S, N_2 and CO_2 in the gas phase were acquired separately in two different spectral windows. The absence of H_2 was monitored in a third spectral window. Peak positions and areas were determined using the integration tool of LabSpec software (Horiba Jobin Yvon) at 4156 cm^{-1} for H_2; 2917 cm^{-1} for CH_4; 2580 cm^{-1} for H_2S liquid; 2331 cm^{-1} for N_2 and the Fermi doublet at 1285 and 1388 cm^{-1} for CO_2 (Burke, 2001). The composition of biphasic inclusions in FD1A was acquired for 4 inclusions. For FD3A, 5 compositions were determined for biphasic inclusion and 8 compositions were determined for monophasic inclusions (Table S-2). The salinity of the fluid inclusions was calculated in single-salt $NaCl$-CO_2-CH_4-N_2-H_2O system using *Clathrates* computer package (Bakker, 1997), by using either (i) the program *ICE* following the equations of Duan *et al.*, (1996) associated with T_m ice and T_m cla when clathrate dissociation occurred in presence of ice, L_{aq} and CO_2 vap,

or (ii) *Q2* program when clathrate dissociation occurred via a Q_2 transition (coexistence of L_{aq}, Cla, CO_2 liq and CO_2 vap), associated with T_m cla and T_h car and on the equations of Thiéry *et al.* (1994).

Results

For FD1A, the observed phase transitions were T_{fm}, T_m ice, T_m cla, and T_h for 17 inclusions (Table S-4). The T_{fm} were difficult to observe because of the small size of the fluid inclusions and the disappearance of the vapour bubble on cooling, leading to a metastable state of the inclusions until the sudden reappearance of the vapour bubble. Seven of the measured inclusions presented the typical double bubble of CO_2 permitting the observation of T_m car and T_h car. The average molar composition of the vapour phase in inclusions is 91.9 ± 3.4 mol % CO_2, 3.2 to 10.7 mol % N_2 and < 1 mol % CH_4. No significant variations were observed between biphasic and triphasic inclusion. The T_{fm} were observed from −21 to –41 °C and the T_h from 118 to over 200 °C. The inclusions with a $T_{fm} \approx -21$ °C presented the lowest T_h, between 118 and 187 °C, compared to the inclusions with a lower T_{fm} which generally presented a T_h over 200 °C. These observations point to the presence of two fluids: one where the salts present in the aqueous phase are made of pure NaCl and one where they are composed of a mixing between NaCl and another salt species. The total salinity was nonetheless calculated considering pure NaCl and varies uniformly between 0.8 and 25.4 weight % in the aqueous solution independently of the salt system. It is moreover important to note that there is no apparent correlation between salinity and volatiles species concentration.

The T_m ice, T_m cla and T_h were observed for 11 biphasic inclusions in FD3A (Table S-4). Vapour and sometimes solid phases in monophasic inclusions appeared at low temperatures (< −120 °C; n = 14). Biphasic fluid inclusion vapours in sample FD3A contained CH_4 from 9.8 up to 50.4 mole percent (Table S-2). H_2S was systematically present from 0.2 to 1.1 mole percent. N_2 could not be distinguished from atmospheric N_2 for half of the inclusions and reached a maximum of 2.4 mole percent. T_{fm} was difficult to observe in this sample and we assumed pure NaCl to calculate the salinity. It is on average 3.3 ± 1.9 weight percent. The T_h were higher than 174 and generally over 200 °C. Monophasic gaseous liquid inclusions are mostly composed of CH_4 (79.5 to 98.9 mole percent with one outlier at 26.2 mole percent), with minor amounts of H_2S of 0.8 ± 0.3 mole percent. N_2 is only present as a trace > 0.6 mol %. The CO_2 content varied between 4.8 and 19.5 mole percent with an outlier at 73.2 mole percent.

Discussion and interpretation

The dominant orientation of fluid inclusions along parallel pseudo-secondary trails in FD1A sample suggests a strong tectonic influence coherent with the long-term pulsed tectonomagmatic event that affected the Imandra-Varzuga rift zone (Chashchin *et al.*, 2008). However, the tectonically influenced-fluid inclusion planes rarely cross the grains boundaries. So, these fluid inclusions are representative of the fluid, including primary noble-gas composition, present

during quartz growth. Our observations attest the preservation of two fluids within the sample. The first one characterised by pure NaCl in the aqueous phase could be assimilated to a seawater-derived fluid. The second one, where the aqueous phase contains a mixture of NaCl and another salt species, could point to a magmatic signature (Heinrich, 2005) and the analysed fluid inclusions represent a mixture between high-salinity high-temperature magmatic fluids and the low-salinity low-temperature seawater. This is in accordance with the xenon isotopic composition, which indicate a mixing between an atmospheric endmember, derived from the seawater-fluid, and a minor mantle contribution, derived from the magmatic fluid.

Sample FD3A presents heterogeneous entrapment with the coexistence of monophasic and biphasic inclusions with a continuum of size of the vapour bubbles, from 20 to 90 % of the total volume. This observation linked with the co-variation of CH_4/CO_2 content, the monophasic liquid inclusions being enriched in the most volatiles species, are solids arguments for boiling and entrapment below the solvus within the H_2O-CH_4-CO_2-H_2S-N_2 system of a single fluid (Diamond, 2003). Contemporaneous recrystallisation induced the loss of some primary and pseudo-secondary fluid inclusions (Kerrich, 1976). No subsequent fluid circulation was noticed by secondary inclusions. The bulk noble gases composition issued from these fluid inclusions thus likely to reflect the composition of the late Palaeoproterozoic as this sample appears to have precipitated from one unique fluid.

Fissiogenic and mantle contribution

Fissiogenic contribution

Production of heavy Xe isotopes can be attributed to the spontaneous fission of ^{238}U (half-life of 4.47 Ga or ^{244}Pu (half-life of 82 Ma; Ozima and Podosek, 2002). We calculated the theoretical production of the isotopes: $^{131,\ 132,\ 134}Xe$ normalised to ^{136}Xe by fission of ^{238}U and ^{244}Pu (rate of production from Alexander *et al.*, 1971; Ragettli *et al.*, 1994). The Xe isotope excess was calculated as Equation S-1:

$$\left(\frac{^{i}Xe}{^{136}Xe}\right)_{excess} = \frac{\left(\frac{^{i}Xe}{^{130}Xe}\right)_{sample} - \left(\frac{^{i}Xe}{^{130}Xe}\right)_{atm}}{\left(\frac{^{136}Xe}{^{130}Xe}\right)_{sample} - \left(\frac{^{136}Xe}{^{130}Xe}\right)_{atm}} \qquad \text{(Eq. S-1)}$$

Associated uncertainties are as Equation S-2:

$$\sigma_{\left(\frac{^{i}Xe}{^{136}Xe}\right)_{sample}} = \left(\frac{^{i}Xe}{^{136}Xe}\right)_{sample} \times \left[\left(\frac{\sigma_{\left(\frac{^{i}Xe}{^{130}Xe}\right)_{sample}}}{\left(\frac{^{i}Xe}{^{130}Xe}\right)_{sample} - \left(\frac{^{i}Xe}{^{130}Xe}\right)_{atm}}\right)^2 + \left(\frac{\sigma_{\left(\frac{^{136}Xe}{^{130}Xe}\right)_{sample}}}{\left(\frac{^{136}Xe}{^{130}Xe}\right)_{sample} - \left(\frac{^{i}Xe}{^{130}Xe}\right)_{atm}}\right)^2\right]^{1/2} \qquad \text{(Eq. S-2)}$$

By plotting ^{238}U and ^{244}Pu fission spectrums in perspective with sample ratios, a ^{238}U origins of the heavy isotopes can be suggested for all our samples (Fig. 1; Fig. S-2)

Mantle Contribution

The excess of ^{129}Xe is thought to show a binary mixing between Archean atmosphere and mantle-derived xenon in our samples such as Equation S-3:

$$\left(\frac{129}{130}\right)_{Sample} = \alpha \left(\frac{129}{130}\right)_{Mantle} + (1-\alpha) \times \left(\frac{129}{130}\right)_{Archean\ atmosphere} \qquad \text{(Eq. S-3)}$$

with α as the fraction of the mantellic ^{130}Xe. The value used for (129/130) $_{Mantle}$ is dependent on whether significant regassing of atmospheric Xe into the deep Earth is assumed to have occurred. Without regassing, we took the value (129/130) $_{Mantle}$ = 14 ± 1 (Marty e*t al.*, 2019). Considering regassing, we assume a MORB-type composition of (129/130) $_{Mantle}$ = 6.92 ± 0.07 (Pető *et al.*, 2013), that is the lowest estimation in the literature (Holland and Ballentine, 2006; Mukhopadhyay, 2012; Parai and Mukhopadhyay, 2021). The calculated mantellic ^{130}Xe contribution is thus an upper limit. From α we calculated the associated (128/130) $_{Expected}$ for FD1A assuming a (128/130) $_{Mantle}$ = 0.51 ± 0.01 (primordial Xe, Ozima and Podosek, 2002). Results are available in Table S-1. Despite the heavy isotope discrepancies between the two bottles of FD1A, the excess of ^{129}Xe is identical for the two bottles (Table S-3) so we considered an equal mantellic contribution. The difference between the excess of $^{131,\ 132,\ 134,\ 136}$Xe is then due to a difference of crustal fissiogenic ^{238}U contribution.

There is potentially a weak positive correlation among individual data in Figure S-4 with all our measurements parallel to the Rayleigh fractionation trend. This imply a similar contribution from mantle gas to the hydrothermal fluids and it does not appear realistic for samples from different locations. Within the uncertainties, the youngest sample from the Ongeluk formation is atmospheric. The excesses of ^{129}Xe in the samples from the Kola Craton (Polisarka and Seidorechka formations) are consistent with the same mantle contribution to the hydrothermal fluids in this location. However, the oldest sample from Seidorechka formation presents higher $^{128,\ 129}$Xe compare to the modern-air and to the Polisarka sample. This stands for a slightly fractionated atmosphere at the time that disappeared within the ≈ 7 million years separating the formation of the 2 samples. Without ^{129}Xe excesses (this study) or deficits (Avice *et al.*, 2017; Marty *et al.*, 2019), the measurements are expected to fall on the Rayleigh fractionation trend through modern air (Fig. S-4).

Supplementary Tables

Table S-1 Estimation of the ^{130}Xe mantellic contribution from two different endmembers composition. The Archean mantle $^{129}Xe/^{130}Xe$ ratio is used to calculate the % mantle without crustal regassing; The MORB $^{129}Xe/^{130}Xe$ ratio is used to calculate the % mantle with atmospheric regassing. 1 - Marty *et al.* (2019); Pepin (2003); 3 - Pető *et al.* (2013); 4 - Ozima and Podosek (2002).

	$^{129}Xe/^{130}Xe$ (2σ)	$^{128}Xe/^{130}Xe$ (2σ)	Without atm regassing		With atm regassing	
			% Mantle	Expected $^{128}Xe/^{130}Xe$ (2σ)	% Mantle	Expected $^{128}Xe/^{130}Xe$
FD1A	6.58 (0.04)	0.475 (0.003)	$0.9^{+0.3}_{-0.4}$	0.474 (0.001)	$16.8^{+7.1}_{-5.0}$	$0.478^{+0.001}_{-0.003}$
Archean Mantle[1,2]	14 (1)	0.507 (0.004)				
MORB[3]	6.92 (0.07)					
Modern air[4]	6.50					

Table S-2 Molar percentage of volatiles species in some fluid inclusions determined by RAMAN spectrometry.

N° inclusion	% molar				
	CO_2	N_2	H_2S	CH_4	Total
FD1A - Biphasic					
13	88.8 %	10.5 %	0.0 %	0.7 %	100.0 %
28	93.4 %	6.5 %	0.0 %	0.1 %	100.0 %
30	95.9 %	3.2 %	0.0 %	0.9 %	100.0 %
31	89.3 %	10.7 %	0.0 %	0.0 %	100.0 %
FD3A - Biphasic					
1	90.0 %	0.0 %	0.2 %	9.8 %	100.0 %
2	60.7 %	2.4 %	0.3 %	36.6 %	100.0 %
3	68.3 %	0.0 %	0.2 %	31.5 %	100.0 %
6	47.7 %	0.8 %	1.1 %	50.4 %	100.0 %
9	59.7 %	0.7 %	0.5 %	39.2 %	100.0 %
21	61.1 %	0.0 %	0.3 %	38.6 %	100.0 %
FD3A - Monophasic					
1	0.0 %	0.0 %	1.1 %	98.9 %	100.0 %
2	0.0 %	0.0 %	1.4 %	98.6 %	100.0 %
3	73.2 %	0.2 %	0.4 %	26.2 %	100.0 %
5	4.8 %	0.0 %	0.8 %	94.4 %	100.0 %
8	16.3 %	0.0 %	0.9 %	82.8 %	100.0 %
13	19.2 %	0.5 %	0.7 %	79.6 %	100.0 %
14	19.5 %	0.5 %	0.5 %	79.5 %	100.0 %
15	15.9 %	0.5 %	0.7 %	82.9 %	100.0 %

Table S-3   Isotopic ratio of the noble gases of each replicate. Values in red are outliers according to the Chauvenet criterion (Anscombe, 1960) and were not taken into account in the calculation of the weighted average.

Table S-4   Observed phase transitions for FD1A biphasic fluid inclusion; FD3A biphasic and monophasic fluid inclusion and calculated NaCl weight percent associated. Value n. o. corresponds to a non-observed phase change.

Tables S-3 and S-4 can be downloaded (Excel) from the online version of the article at https://doi.org/10.7185/geochemlet.2207.

Supplementary Figures
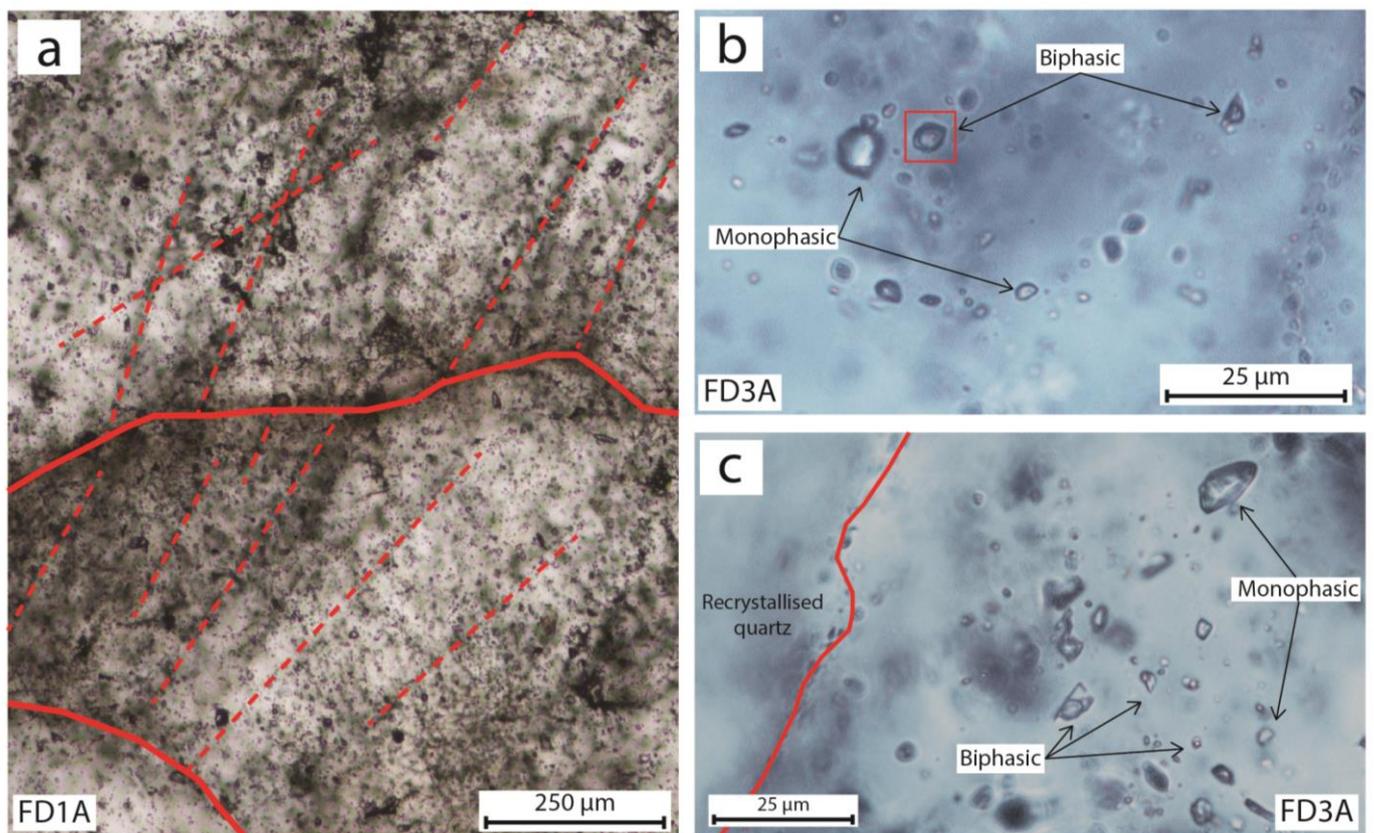
Figure S-1   **(a)** Thin section photographs highlighting quartz grain boundaries (solid lines) and trails of pseudosecondary fluid inclusions (dashed lines) in FD1A. **(b)** Coexisting monophasic and biphasic fluid inclusions in FD3A. The red square shows a biphasic inclusion with a small rim of liquid. **(c)** Hetereogeneous entrapment in a fluid inclusion assemblage showing the coexistence of monophasic and biphasic inclusions with variable % of vapour in FD3A characteristic of boiling process. The grain on the left is devoid of fluid inclusions as a result of recrystallisation.
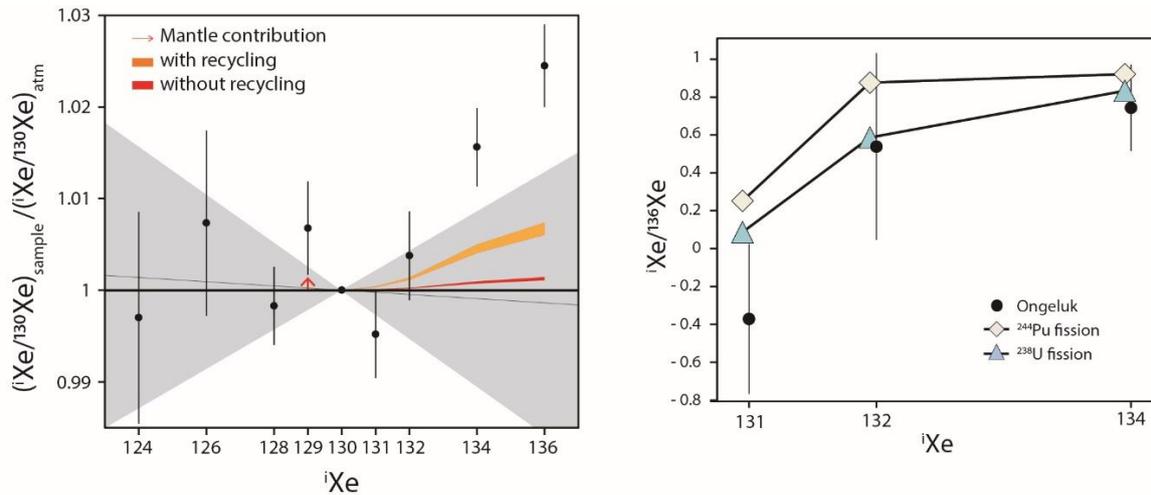
Figure S-2   Isotopic spectra of Xe released from fluid inclusions in samples from the Ongeluk fm. Points represent the weighted average of 9 crushes of different quartz samples from the Ongeluk fm with error at 1σ. The grey line corresponds to the isotopic trend of the $^{124, 126, 128, 130}$Xe showing no mass-dependant fractionation. Error envelope is at 2σ. The mantellic contribution is calculated considering a starting atmospheric composition as no isotopic fractionation is observed. The associated fission spectrum shows the major influence of ^{238}U spontaneous fission with uncertainties at 1σ.
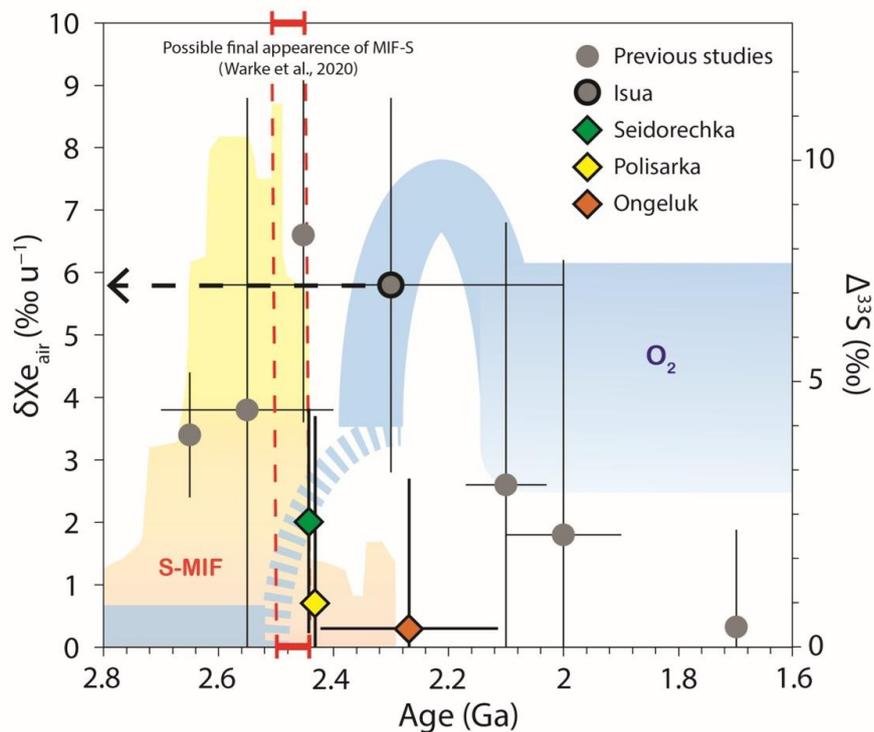

Figure S-3   Records of atmospheric oxygen (O$_2$, blue; Lyons *et al.*, 2014), mass-independent fractionation of sulfur isotopes (MIF-S, orange; data from Killingsworth *et al.*, 2019) and mass dependent fractionation of xenon isotopes over the GOE period (previous data from Avice *et al.*, 2018; Almayrac *et al.*, 2021), errors are at 2σ.
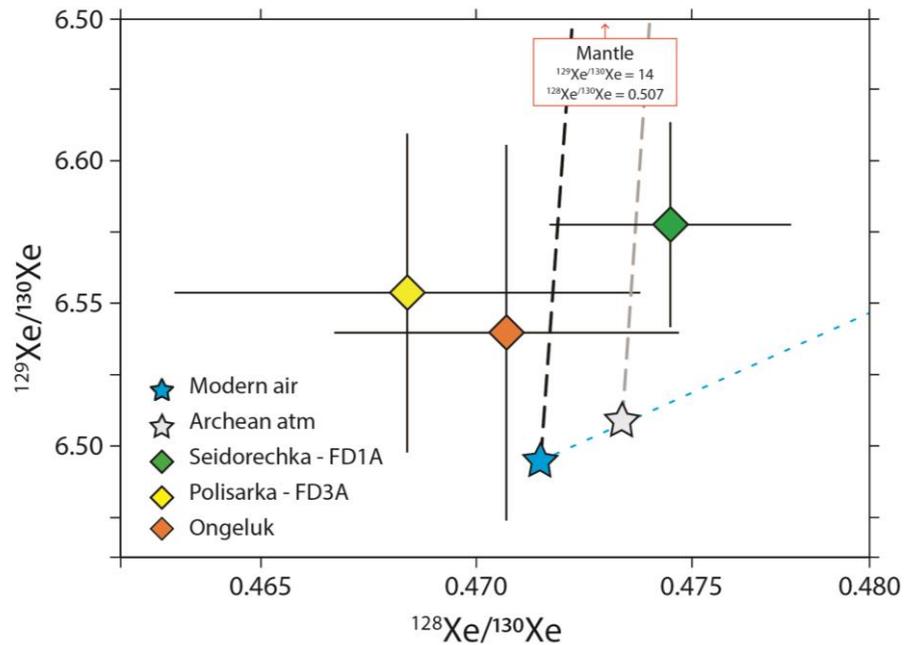
Figure S-4   Isotopic ratios $^{129}Xe/^{130}Xe$ vs. $^{128}Xe/^{130}Xe$ in this study. The black (a) and grey (b) dashed lines show a mixing between a non-regassed mantle and: (a) the modern air (Ozima and Podosek, 2002); (b) the Archean atmospheric ratio calculated from FD1A. Mantle $^{129}Xe/^{130}Xe$ composition comes from Marty *et al.* (2019) and AVCC-like $^{128}Xe/^{130}Xe$ (Pepin, 2003). The blue dashed line shows a Rayleigh fractionation trend through modern air. Uncertainties at 2σ.

Supplementary Information References

Alexander, E.C., Lewis, R.S., Reynolds, J.H., Michel, M.C. (1971) Plutonium-244: Confirmation as an Extinct Radioactivity. *Science* 172, 837-840. https://doi.org/10.1126/science.172.3985.837

Almayrac, M.G., Broadley, M.W., Bekaert, D.V., Hofmann, A., Marty, B. (2021) Possible discontinuous evolution of atmospheric xenon suggested by Archean barites. *Chemical Geology* 581, 120405. https://doi.org/10.1016/j.chemgeo.2021.120405

Amelin, Y.V., Heaman, L.M., Semenov, V.S. (1995) U-Pb geochronology of layered mafic intrusions in the eastern Baltic Shield : Implications for the timing and duration of Paleoproterozoic continental rifting. *Precambrian Research* 75, 31-46. https://doi.org/10.1016/0301-9268(95)00015-W

Anscombe, F.J. (1960) Rejection of Outliers. *Technometrics* 2, 123-146. https://doi.org/10.1080/00401706.1960.10489888

Avice, G., Marty, B., Burgess, R. (2017) The origin and degassing history of the Earth's atmosphere revealed by Archean xenon. *Nature Communications* 8, 15455. https://doi.org/10.1038/ncomms15455

Avice, G., Marty, B., Burgess, R., Hofmann, A., Philippot, P., Zahnle, K., Zakharov, D. (2018) Evolution of atmospheric xenon and other noble gases inferred from Archean to Paleoproterozoic rocks. *Geochimica et Cosmochimica Acta* 232, 82-100. https://doi.org/10.1016/j.gca.2018.04.018

Bakker, R.J. (1997) Clathrates : Computer programs to calculate fluid inclusion V-X properties using clathrate melting temperatures. *Computers & Geosciences* 23, 1-18. https://doi.org/10.1016/S0098-3004(96)00073-8

Brasier, A.T., Martin, A.P., Melezhik, V.A., Prave, A.R., Condon, D.J., Fallick, A.E. (2013) Earth's earliest global glaciation? Carbonate geochemistry and geochronology of the Polisarka Sedimentary Formation, Kola Peninsula, Russia. *Precambrian Research* 235, 278-294. https://doi.org/10.1016/j.precamres.2013.06.007

Burke, E.A.J. (2001) Raman microspectrometry of fluid inclusions. *Lithos* 55, 139-158. https://doi.org/10.1016/S0024-4937(00)00043-8

Chashchin, V.V., Bayanova, T.B., Levkovich, N.V. (2008) Volcanoplutonic association of the early-stage evolution of the Imandra-Varzuga rift zone, Kola Peninsula, Russia: Geological, petrogeochemical, and isotope-geochronological data. *Petrology* 16, 279-298. https://doi.org/10.1134/S0869591108030041

Cornell, D.H., Schütte, S.S., Eglington, B.L. (1996) The Ongeluk basaltic andesite formation in Griqualand West, South Africa : Submarine alteration in a 2222 Ma proterozoic sea. *Precambrian Research* 79, 101-123. https://doi.org/10.1016/0301-9268(95)00090-9

Diamond, L.W. (2003) Introduction to gas-bearing, aqueous fluid inclusions. *Fluid inclusions: analysis and interpretation* 32, 101-158.

Duan, Z., Møller, N., Weare, J.H. (1996) A general equation of state for supercritical fluid mixtures and molecular dynamics simulation of mixture PVTX properties. *Geochimica et Cosmochimica Acta* 60, 1209-1216. https://doi.org/10.1016/0016-7037(96)00004-X

Eglinger, A., Ferraina, C., Tarantola, A., André-Mayer, A.S., Vanderhaeghe, O., Boiron, M.C., Dubessy, J., Richard, A., Brouand, M. (2014) Hypersaline fluids generated by high-grade metamorphism of evaporites : Fluid inclusion study of uranium occurrences in the Western Zambian Copperbelt. *Contributions to Mineralogy and Petrology* 167, 967. https://doi.org/10.1007/s00410-014-0967-9

Gumsley, A.P., Chamberlain, K.R., Bleeker, W., Söderlund, U., de Kock, M.O., Larsson, E.R., Bekker, A. (2017) Timing and tempo of the Great Oxidation Event. *Proceedings of the National Academy of Sciences* 114, 1811-1816. https://doi.org/10.1073/pnas.1608824114

Gutzmer, J., Pack, A., Lüders, V., Wilkinson, J., Beukes, N., Niekerk, H. (2001) Formation of jasper and andradite during low-temperature hydrothermal seafloor metamorphism, Ongeluk Formation, South Africa. *Contributions to Mineralogy and Petrology* 142, 27-42. https://doi.org/10.1007/s004100100270

Gutzmer, J., Banks, D.A., Lüders, V., Hoefs, J., Beukes, N.J., von Bezing, K.L. (2003) Ancient sub-seafloor alteration of basaltic andesites of the Ongeluk Formation, South Africa : Implications for the chemistry of Paleoproterozoic seawater. *Chemical Geology* 201, 37-53. https://doi.org/10.1016/S0009-2541(03)00225-0

Heinrich, C.A. (2005) The physical and chemical evolution of low-salinity magmatic fluids at the porphyry to epithermal transition : A thermodynamic study. *Mineralium Deposita* 39, 864-889. https://doi.org/10.1007/s00126-004-0461-9

Holland, G., Ballentine, C.J. (2006) Seawater subduction controls the heavy noble gas composition of the mantle. *Nature* 441, 186-191. https://doi.org/10.1038/nature04761

Holland, H.D. (2006) The oxygenation of the atmosphere and oceans. *Philosophical Transactions of the Royal Society B: Biological Sciences* 361, 903-915. https://doi.org/10.1098/rstb.2006.1838

Kerrich, R. (1976) Some effects of tectonic recrystallisation on fluid inclusions in vein quartz. *Contributions to Mineralogy and Petrology* 59, 195-202. https://doi.org/10.1007/BF00371308

Killingsworth, B.A., Sansjofre, P., Philippot, P., Cartigny, P., Thomazo, C., Lalonde, S.V. (2019) Constraining the rise of oxygen with oxygen isotopes. *Nature Communications* 10, 4924. https://doi.org/10.1038/s41467-019-12883-2

Lyons, T.W., Reinhard, C.T., Planavsky, N.J. (2014) The rise of oxygen in Earth's early ocean and atmosphere. *Nature* 506, 307-315. https://doi.org/10.1038/nature13068

Marty, B., Bekaert, D.V., Broadley, M.W., Jaupart, C. (2019) Geochemical evidence for high volatile fluxes from the mantle at the end of the Archaean. *Nature* 575, 485-488. https://doi.org/10.1038/s41586-019-1745-7

Melezhik, V.A., Sturt, B.A. (1994) General geology and evolutionary history of the early proterozoic Polmak-Pasvik-Pechenga-Imandra/Varzuga-Ust'Ponoy greenstone belt in the northeastern Baltic Shield. *Earth-Science Reviews* 36, 205-241. https://doi.org/10.1016/0012-8252(94)90058-2

Melezhik, V.A., Prave, A.R., Lepland, A., Hanski, E.J., Romashkin, A.E., Rychanchik, D.V., Luo, Z.Y., Sharkov, E.V., Bogina, M.M., Brasier, A.T., Fallick, A.E. (2013) 6.1 The Imandra/Varzuga Greenstone Belt. In: Melezhik, V., Prave, A.R., Hanski, E.J., Fallick, A.E., Lepland, A., Kump, L.R., Strauss, H. (Eds.) *Reading the Archive of Earth's Oxygenation*. Springer Berlin Heidelberg, 505-590. https://doi.org/10.1007/978-3-642-29659-8_2

Mukhopadhyay, S. (2012) Early differentiation and volatile accretion recorded in deep-mantle neon and xenon. *Nature* 486, 101-104. https://doi.org/10.1038/nature11141

Ozima, M., Podosek, F.A. (2002) *Noble Gas Geochemistry*. Second Edition, Cambridge University Press, Cambridge. https://doi.org/10.1017/CBO9780511545986

Parai, R., Mukhopadhyay, S. (2021) Heavy noble gas signatures of the North Atlantic Popping Rock 2ΠD43 : Implications for mantle noble gas heterogeneity. *Geochimica et Cosmochimica Acta* 294, 89-105. https://doi.org/10.1016/j.gca.2020.11.011

Pepin, R.O. (2003) On Noble Gas Processing in the Solar Accretion Disk. In: Kallenbach, R., Encrenaz, T., Geiss, J., Mauersberger, K., Owen, T.C., Robert, F. (Eds.) *Solar System History from Isotopic Signatures of Volatile Elements:*

Volume Resulting from an ISSI Workshop 14–18 January 2002, Springer Netherlands, Bern, 211-230. https://doi.org/10.1007/978-94-010-0145-8_14

Péron, S., Moreira, M. (2018) Onset of volatile recycling into the mantle determined by xenon anomalies. *Geochemical Perspectives Letters* 9, 21-25. https://doi.org/10.7185/geochemlet.1833

Pető, M.K., Mukhopadhyay, S., Kelley, K.A. (2013) Heterogeneities from the first 100 million years recorded in deep mantle noble gases from the Northern Lau Back-arc Basin. *Earth and Planetary Science Letters* 369-370, 13-23. https://doi.org/10.1016/j.epsl.2013.02.012

Ragettli, R A., Hebeda, E.H., Signer, P., Wieler, R. (1994) Uranium-xenon chronology: Precise determination of $\lambda s f \ast 136 Y s f$ for spontaneous fission of 238U. *Earth and Planetary Science Letters* 128, 653-670. https://doi.org/10.1016/0012-821X(94)90177-5

Roedder, E. (1984) *Fluid inclusions.* Reviews in Mineralogy, Vol. 12. Mineralogical Society of America, Virginia.

Saito, T., Shibuya, T., Komiya, T., Kitajima, K., Yamamoto, S., Nishizawa, M., Ueno, Y., Kurosawa, M., Maruyama, S. (2016) PIXE and microthermometric analyses of fluid inclusions in hydrothermal quartz from the 2.2Ga Ongeluk Formation, South Africa : Implications for ancient seawater salinity. *Precambrian Research* 286, 337-351. https://doi.org/10.1016/j.precamres.2016.10.003

Saito, T., Qiu, H.N., Shibuya, T., Li, Y.B., Kitajima, K., Yamamoto, S., Ueda, H., Komiya, T., Maruyama, S. (2018) Ar–Ar dating for hydrothermal quartz from the 2.4 Ga Ongeluk Formation, South Africa : Implications for seafloor hydrothermal circulation. *Royal Society Open Science* 5, 180260. https://doi.org/10.1098/rsos.180260

Thiéry, R., Kerkhof, A., Dubessy, J. (1994) vX properties of CH4-CO2 and CO2-N2 fluid inclusions : Modelling for T <31°C and P <400 bars. *European Journal of Mineralogy* 6, 753-771. https://doi.org/10.1127/ejm/6/6/0753

Vermeesch, P. (2018) IsoplotR : A free and open toolbox for geochronology. *Geoscience Frontiers* 9, 1479-1493. https://doi.org/10.1016/j.gsf.2018.04.001

Warke, M.R., Di Rocco, T., Zerkle, A.L., Lepland, A., Prave, A.R., Martin, A.P., Ueno, Y., Condon, D.J., Claire, M.W. (2020) The Great Oxidation Event preceded a Paleoproterozoic "snowball Earth". *Proceedings of the National Academy of Sciences* 117, 13314-13320. https://doi.org/10.1073/pnas.2003090117